

# Transmission electron microscopy applied to fluid inclusion investigations

Cecilia Viti<sup>\*</sup>, Maria-Luce Frezzotti

*Dipartimento di Scienze della Terra, Via Laterina 8, 53100 Siena, Italy*

Received 15 March 1999; accepted 28 April 2000

---

## Abstract

The transmission electron microscope (TEM) allows a detailed characterization of textural and chemical features of fluid inclusions (shape, inner compositions and inner textures), at a resolution higher than that attainable with an optical microscope (OM). TEM investigation indicates that most fluid inclusions appear as perfectly euhedral negative crystals, with variable shape (from prismatic to equant) and size (typically from  $< 0.02$  to  $0.15 \mu\text{m}$ ). Inner texture (fluid phase/melt distribution) and composition are variable as well. Different kinds of negative crystals may coexist in the same trail of inclusions, possibly indicating locally variable trapping conditions.

A critical feature, revealed by TEM, is that inclusions are often connected to structural defects (in particular, to dislocation arrays), which are undetected by optical microscopy. The identification of these hidden nanostructures should be taken into account for the correct petrological interpretation of microthermometric results, particularly when controversial data have been obtained. In fact, these nanostructures may represent a possible path for fluid phase leakage, thus modifying the original composition and/or density of the inclusions. © 2001 Elsevier Science B.V. All rights reserved.

*Keywords:* TEM; Fluid inclusions; Negative crystals; Dislocations; Leakage; Re-equilibration

---

## 1. Introduction

The transmission electron microscope (TEM) methods have been proven to be highly successful for investigating structures (crystal order–disorder, twinning, defects, dislocations and polytypism) nanostructures (relations between different crystals and/or minerals, solid-state reactions and fine intergrowths) and chemical characters of single minerals, with a spatial and analytical resolution higher than most other instruments.

TEM can be applied to different mineralogical, petrological and geochemical problems. Melt and fluid inclusions may represent a possible field of interest: inclusions often are less than a few microns in size, most of them are well below the optical resolution and many related details are not always revealed at the optical scale. Finally, the small size of daughter phases present within inclusions often preclude chemical analyses by conventional techniques, such as energy and wavelength dispersive spectroscopies (EDS and WDS, respectively) in the scanning electron microscopy mode (SEM).

Nevertheless, TEM has rarely been employed in melt and fluid inclusion investigations, possibly because the instrument is expensive and its proper use

---

<sup>\*</sup> Corresponding author. Fax: +39-577-233938.

*E-mail addresses:* vitic@unisi.it (C. Viti), frezzottiml@unisi.it (M.-L. Frezzotti).

requires a general knowledge on crystallography, diffraction, scattering processes and spectroscopy. At present, there are very few dedicated references: mineral inclusions have been reported in some TEM studies in olivine and quartz (e.g. McLaren et al., 1983; FitzGerald et al., 1991) but only a few papers are specifically addressed to them. An extensive study, dealing with the re-equilibration of  $H_2O + CO_2$  inclusions in synthetic quartz is represented by the paper of Bakker and Jansen (1994). Green and Radcliffe (1975), in their study on fluid precipitates in mantle olivine and pyroxene, described very small  $CO_2$ -rich bubbles, attached to crystal defects induced by deformation (dislocations), exsolution (in pyroxenes) and grain boundaries. Recently, the occurrence of melt and fluid inclusions in mantle olivines has

also been discussed by Viti and Frezzotti (2000): most of those observations will be reported in this chapter.

## 2. The TEM

Spence (1981), Buseck et al. (1988) and Williams and Carter (1996) and references therein provide detailed information on electron diffraction, imaging and related spectroscopic techniques. Examples of TEM studies specifically devoted to mineralogy can be found in Veblen (1985), Mellini (1989) and Buseck (1992).

The TEM can be compared to the petrographic optical microscope (OM), with which all petrologists

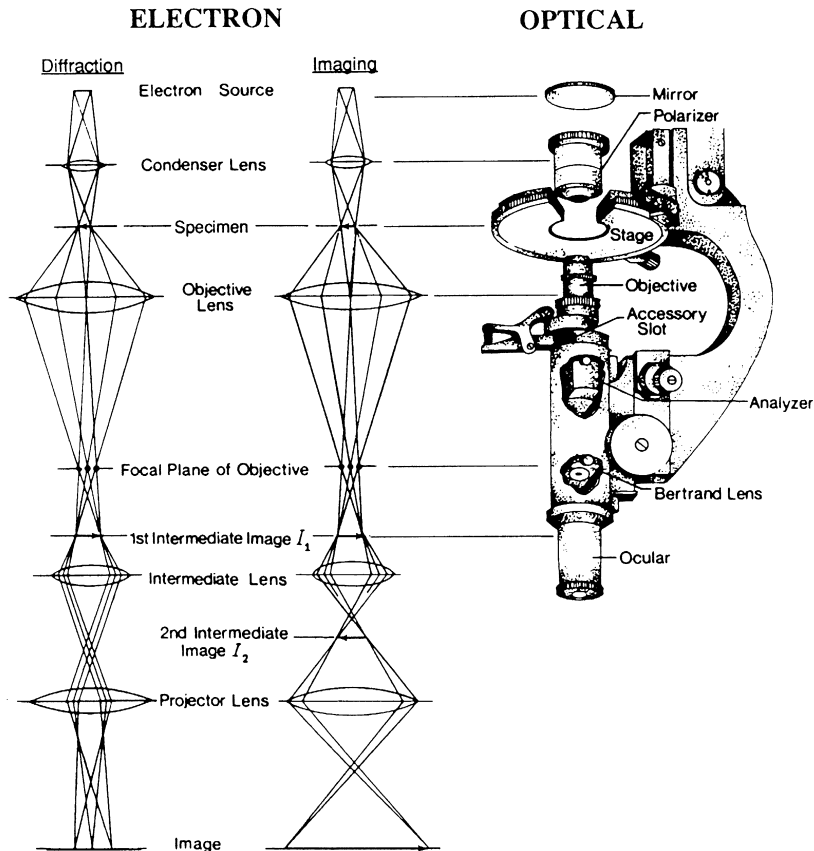


Fig. 1. Comparison between TEM and OM. The two ray diagrams correspond to diffraction and imaging modes, respectively. Figure from Buseck (1992).

are familiar (Fig. 1). The essential components are: a light source (emitting electrons rather than visible light); a beam, travelling along the microscope column through a thin transparent specimen (thickness of  $\sim 100\text{--}1000 \text{ \AA}$  compared to the typical  $30 \mu\text{m}$  of petrographic sections); and a lens system (electromagnetic rather than optical lenses), which controls the beam path down to the image plane. Both electron and OM provide enlarged images of the object (with magnifications greater than 1 million in the TEM) and interference pattern (the interference figure in the OM and the electron diffraction pattern in the TEM).

The beam, emitted by the electron gun (W filament,  $\text{LaB}_6$  crystal or field emission gun (FEG)), is ideally monochromatic. Its wavelength depends on the accelerating voltage of the microscope (from 100 up to 1000 kV): the higher the voltage, the lower the beam wavelength and the higher the microscope resolution. Unfortunately, the microscope resolution is strongly reduced by lens aberrations, the most critical of which is the spherical aberration of the objective lens. The general expression for resolution is then  $r = 0.67\lambda^{3/4}C_s^{1/4}$  (where  $r$  is resolution,  $\lambda$  is the beam wavelength and  $C_s$  is the spherical aberration coefficient): with a microscope voltage of 120 kV and a corresponding wavelength of electrons  $0.032 \text{ \AA}$ , the resolution is about  $4 \text{ \AA}$ . In modern microscopes (working at higher voltages, typically 200–400 kV, and with improved optical lens performances), resolutions may be  $2 \text{ \AA}$  or better, then approaching the atomic resolution.

The electron beam is focussed onto the specimen by the condenser lenses (Fig. 1). The interaction between the high-energy incident electrons and the specimen produces many different signals: among these, elastically scattered electrons (i.e. diffracted beams) give rise to diffraction patterns and images; other signals, due to inelastic processes are detected and used for chemical analysis (in particular, electrons for electron energy loss spectroscopy (EELS) and characteristic X-rays for EDS).

At the specimen exit surface, the diffracted beams are collected by the objective lens and transferred through the intermediate and projector lenses down to the viewing screen, where the diffraction pattern or the corresponding image can be observed. Moving from image (real space) to diffraction (reciprocal

space) is immediate, simply by changing the optics of the intermediate lenses.

### 2.1. Electron diffraction

The incident wave is elastically scattered by the atoms of the specimen: positive interferences of the scattered waves give rise to the diffracted beams and, consequently, to maxima in diffraction patterns.

Since electrons interact with both the negative electron cloud and the positive nucleus, the scattering factors for electrons are higher than for X-rays, which are scattered only by the negative potential. Electron diffraction is  $10^8$  times more intense than X-ray diffraction. This has several advantages: for instance, reflections that are weak to X-rays become intense in electron diffraction, even from extremely small volumes. Electron diffraction patterns are formed immediately during observation: crystals can be tilted and precisely oriented with respect to the incident beam from their diffraction patterns. On the other hand, the strength of electron–matter interactions may complicate the electron diffraction pattern. In particular, the intensity of diffracted beams cannot be explained simply in terms of kinematical theory (that is, intensity proportional to the squared amplitude, as in X-rays) and it is affected also by dynamical contributions. This means that the high-energy diffracted beams may behave as new incident beams while travelling through the specimen, giving rise to additional scattering episodes (Cowley, 1981).

On the basis of the convergence angle of the incident beam, mostly two diffraction techniques are used: (1) selected area electron diffraction (SAED), with parallel incident waves, and (2) convergent beam electron diffraction (CBED). In the SAED mode, the diffracting area is selected by the insertion of an aperture, as small as  $0.5 \mu\text{m}$  in diameter: the corresponding diffraction pattern represents an undistorted bidimensional view of the reciprocal lattice (Fig. 2a), holding information on 2D symmetry and lattice parameters, crystal order–disorder (sharp, splitted or diffuse reflections), modulations (polytypism and polysomatism), twinning, topotactic relations and so on. Fig. 2b shows a SAED pattern of a polycrystalline sample: the radius of each diffraction ring corresponds to the characteristic spacings of the diffracting crystals (so that we can obtain a list of

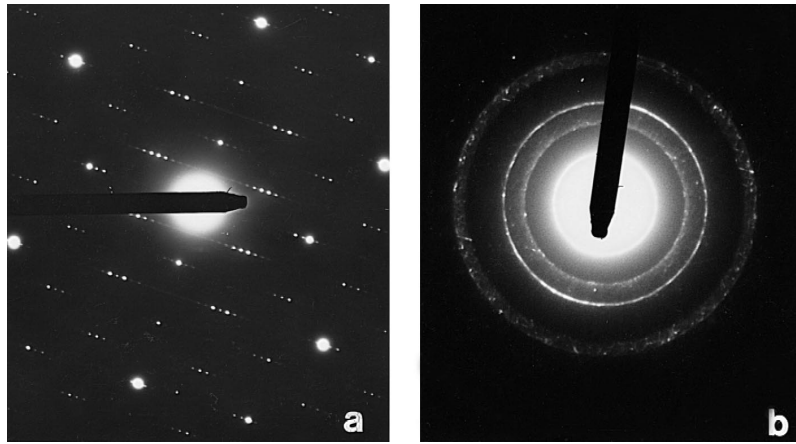


Fig. 2. (a)  $a^* b^*$  electron diffraction pattern of an antigorite single crystal. The satellite reflections, clustered around the main reflections, are due to the antigorite polysomatic modulation. (b) Electron diffraction pattern of a polycrystalline sample.

d-spacings as in X-rays powder diffraction). The main limitations of SAED are the limited spatial resolution (crystallites are often even less than 0.5  $\mu\text{m}$  in diameter) and the lack of 3D information.

CBED overcomes these limitations. The diffracting area, selected by focussing the incident beam (no longer parallel) onto the specimen, is less than 50  $\text{\AA}$  in diameter. Owing to the convergence of the incident beam, the CBED pattern consists of disks, rather than spots, containing several inner contrast features. Leaving out the complex details of CBED and relative processing methods (Steeds and Morniroli, 1992; Gjønnes, 1997; Tanaka, 1997), we just recall that CBED allows accurate measures of 3D symmetry and lattice parameters (determination of the space group), together with an estimate of specimen thickness.

## 2.2. Imaging: amplitude and phase contrast

Contrary to X-rays, which cannot be focused to produce X-ray images, the electron waves can be adequately combined by the electromagnetic lenses to form images. Depending on the number and on the character of the diffracted waves contributing to the image, two kinds of image contrast can be obtained: amplitude and phase contrast.

In amplitude contrast images, only one beam is selected (by the insertion of a small objective aperture): the transmitted beam gives rise to bright field

images, whereas dark field images are obtained from any diffracted beam. Dark field images are useful to produce highly contrasted pictures of heterogeneous systems, e.g. when two different phases, crystal orientations and/or structures are closely associated, as in the case of fine intergrowths, twinings and antiphase domains. In the SAED pattern of a two-phase (A and B) intergrowth, only one spot (due to A or B) can be suitably selected: dark field images, formed from a diffracted beam of A, will show A lighter with respect to B, thus outlining the fine intergrowth texture.

In phase contrast, both transmitted and diffracted beams contribute to the image. Depending on many factors (among which magnification, number of selected beams, d-spacings and microscope resolution), different images can be obtained. Fig. 3a shows a low magnification image of a serpentine specimen: white areas (upper left corner) represent voids where the incident beam has been transmitted without scattering episodes; different grey tones represent the solid material. In general, darker contrast corresponds to thicker areas and/or to higher mean atomic number.

Phase contrast images may exhibit (usually at high magnification) 1D lattice fringes (providing information on the lattice spacings) or bidimensional high-resolution images (which can provide further information on the crystal structure). Fig. 3b shows a lattice fringes image of a chrysotile fibre, perpendicular

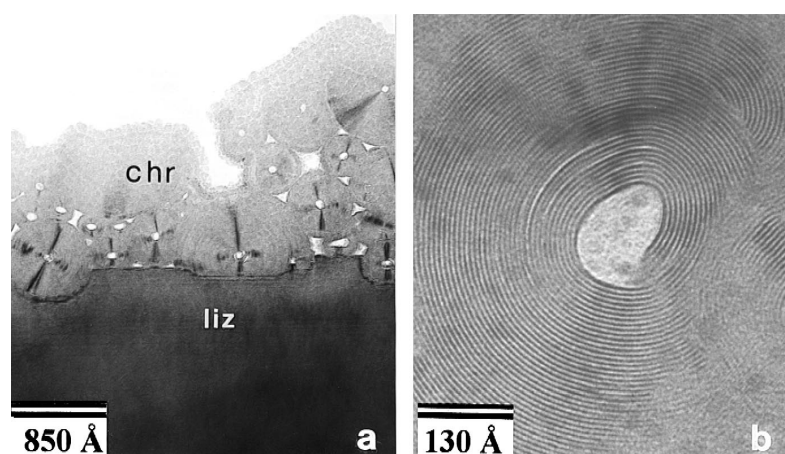


Fig. 3. (a) Low magnification TEM image of the reaction front between a lizardite crystal (liz) and chrysotile fibres (chr). (b) Lattice fringe image of a chrysotile fibre, perpendicular to the fibre axis.

ular to the fibre axis: fringes, whose spacing is approximately 7 Å, correspond to the (001) planes of serpentine. Bidimensional high-resolution images roughly consist of a periodic array of black dots (corresponding to atom columns) and of white dots (corresponding to low deflecting potential areas): in ideal conditions, these images can be considered as a projection of the crystal structure. We must always keep in mind, however, that the interpretation of high-resolution images in terms of crystal structure is not immediate: several parameters (thickness, incorrect defocus, dynamical contributions and crystal misorientation) may complicate the image contrast, introducing different kinds of artifacts (contrast reversal, false periodicities and so on). A possible solution to the problem is represented by image simulation starting from a known structural model. Different images of the starting model are produced at variable thickness and defocus values (so the same crystal structure may give rise to very different images); both the microscope specimen parameters and the starting structural model can be changed until the best fit is found (O'Keefe et al., 1978; Spence, 1981; Self, 1992; Dorset et al., 1997).

### 2.3. Chemical analysis: EDS and EELS

When a high-energy electron inelastically interacts with a target atom, the amount of transferred

energy may cause the ejection of electrons from the inner shells. The ionized atom returns to its ground state by electron transitions from the outer to the inner shells. Each transition produces emission of X-rays, whose energy is directly related to the energy difference between the shells involved in the transition. As a consequence, X-rays are characteristic of the target atom and may be used for qualitative and quantitative chemical analyses (by either EDS and WDS spectrometry).

The principles of EDS are the same in TEM and SEM modes. Major differences arise from the raw data treatment, essentially due to the different specimen thickness: in thin specimens, the effects of absorption and fluorescence can be neglected and only a  $Z$  (atomic number) correction must be taken into account. The method used for chemical determination of thin films, proposed by Cliff and Lorimer (1975), involves the determination of proportionality factors  $K_{A/B}$  (atom A with respect to atom B, typically, Si when studying silicates), on the basis of standard compounds of known composition. These factors are applied to the experimental intensity ratios to obtain atomic concentrations (e.g. Mellini and Menichini, 1985; Peacor, 1992). The main limitation of TEM EDS data is that they are not rigorously quantitative: in particular they cannot be considered as absolute, since the specimen thickness varies from point to point and the analyzed volume (not constant as in SEM) cannot be estimated.

TEM EDS offers great analytical resolution. Beam broadening effects, typically occurring in thick specimens, can be neglected; moreover, the electron beam can be condensed to obtain very fine spots (less than 50 Å in conventional microscopes and a few ångströms in dedicated STEM, compared to the typical beam size of 3–5 µm in SEM). Consequently, the minimum analytical volume is several orders of magnitude lower than in SEM. This could have important implications for inclusions studies, particularly when pure analyses of the inner phases are requested: SEM EDS and WDS compositions obtained from inclusions less than 10 µm in diameter are reasonably affected by contamination of the host mineral.

EELS detects the energy loss of electrons with respect to the incident energy at the specimen exit surface. In particular, it measures the amount of energy transferred to the specimen atoms, necessary to their ionization: EELS is then complementary to EDS. Since the energy loss is characteristic of the inner shell binding energy, EELS provide qualitative and quantitative data and is specifically applied to the chemical analysis of light elements (small energy losses). EELS spectra also contain many other fine structures which can give information on the oxidation state and the coordination of each element (Williams and Carter, 1996, vol. IV).

### 3. Applications to fluid inclusion studies

#### 3.1. Specimen preparation

Specimen preparation is time consuming and critical. It must be carried out with great care since only well prepared specimens will give interpretable results. An additional point of paramount importance is the specimen representativity. This last is a general problem in geology, but it becomes particularly severe in TEM investigations, where only a few square microns of the selected specimen are analyzed. It has been estimated that only 0.6 mm<sup>3</sup> of material has been investigated since the first TEM became available (Williams and Carter, 1996). Therefore, a careful sampling strategy is recommended and it is advisable to prepare at least two or three different TEM grids for the same problem, especially in those het-

erogeneous samples (e.g. showing a heterogeneous distribution of fluid inclusions).

The final aim is to make thin electron-transparent specimens, less than 1000 Å thick (ideally 100 Å). There are mainly two kinds of preparation techniques: fine grinding of rock/crystal fragments (using mesh grids) and ion thinning of specimens selected from petrographic sections (using grids with a central hole). In the first case, sample preparation is quite easy, but most of nanotextural information (for instance, the relationships among different grains) is lost. Another common drawback is preferred orientation, particularly while studying minerals with a strong cleavage: for instance, powder grids of layer silicates bring nice, transparent (001) foils, but all the information about the stacking sequence along [001] axis is lost. On the other hand, small and still thick grains are often obtained by grinding minerals without a marked cleavage.

The ion thinning technique preserves all nanotextural information on oriented crystals and it is recommended in mineral and fluid inclusion studies. The interest area in the specimen (a single crystal, a boundary between two different minerals, a fine intergrowth, an inclusion trail, etc.) is extracted at the OM from a petrographic section and thinned by an Ar<sup>+</sup> accelerated beam, until electron-transparent areas are produced. Fig. 4 shows a back-scattered (BSE) image of a thinned olivine crystal. The specimen is electron-transparent only around the central hole. The degree of thinning can also be checked at the OM, on the basis of the birefringence colors: for instance, the birefringence of the olivine in Fig. 4 changes from yellow (second order) to grey (first order), moving from the edge of the grid towards the central thinning hole.

The need of very thin specimens may represent a drawback in fluid and melt inclusion investigations: inclusions larger than 1 µm in diameter are frequently disturbed during thinning, with a consequent collapse of the solid (glass or mineral) and loss of the fluid phases.

#### 3.2. Size, shape and internal texture of inclusions and negative crystals

At the TEM scale, melt and fluid inclusions may show variable size, shape and internal texture, even

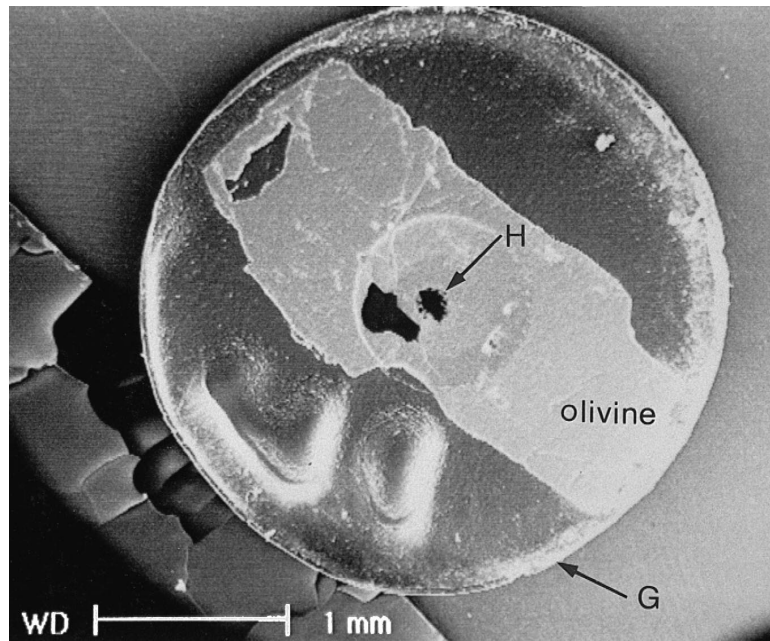


Fig. 4. BSE image of a thinned specimen. G = TEM copper grid (3 mm in diameter, central hole of  $\sim 800 \mu\text{m}$ ), H = hole produced by  $\text{Ar}^+$  thinning.

within the same trail. While comparing different inclusions, we must always consider that the information is strictly bidimensional. Consequently, differences in inclusion size, shape and inner texture can be due to different sectioning levels of the inclusions. Another feature to be considered is the

orientation of the host mineral: rigorously, inclusions should be compared in the same host crystal orientation.

Typical inclusion size ranges from less than  $0.02 \mu\text{m}$  up to  $0.30 \mu\text{m}$ , whereas the identification of larger inclusions is quite difficult: usually these last ones

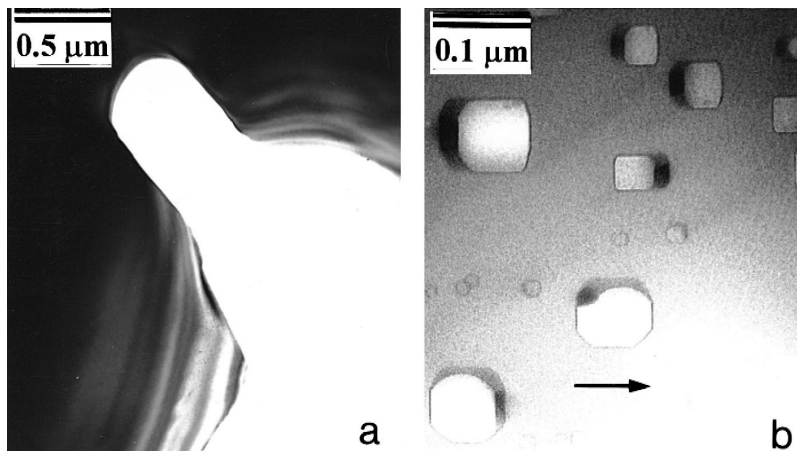


Fig. 5. (a) Low magnification image of a large inclusion in olivine. (b) Negative crystals in olivine; the arrow indicates olivine [100]. Sample from Tenerife xenolith TF14-48.

are broken, empty, appearing as a regular indentation in the crystal thinned edge (Fig. 5a). Thus, size may represent a problem: inclusions studied and measured at the OM rarely correspond to those observed at the TEM. This problem can be overcome by carefully studying the textural characters of the different generations of fluid inclusions: inclusions sharing the same textural characters (e.g. distribu-

tion, shape, inner texture and composition) will correspond to a single population (i.e. the same origin) independently from their absolute size.

Melt and fluid inclusions appear as euhedral negative crystals, that is their shape and orientation are imposed by the host mineral symmetry (Fig. 5b). The occurrence of negative crystals at the TEM scale was already documented by Green and Radcliffe

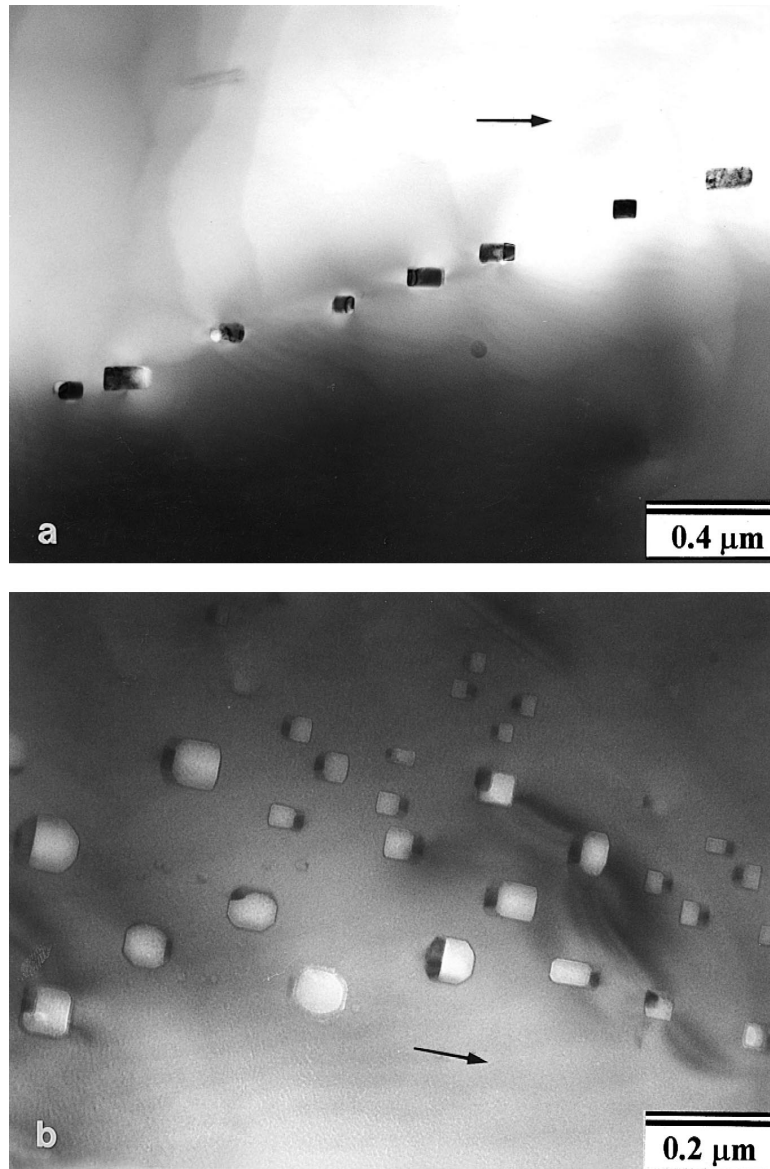


Fig. 6. (a) Trail of prismatic melt inclusions. (b) 'Swarm-shaped' trail. Arrows indicate olivine [100]. Same sample of Fig. 5.

(1975) which reported the occurrence of CO<sub>2</sub> bubbles in mantle olivines, with shapes from rounded to crystallographically controlled (see, for instance, Fig. 4c in their paper). Negative crystals in olivine from a carbonaceous chondrite were also documented by Akai (1994), who suggested that thermal metamorphism was responsible for this ‘void structure’.

Negative crystal shaped inclusions represent a common feature also in mantle olivines from the Canary Islands (Viti and Frezzotti, 2000). Mostly two kinds of trails have been identified: the first kind is represented by regular trails (Fig. 6a), parallel to the olivine [100] and showing a stepwise pattern; these trails consist of prismatic inclusions with a constant size (typically,  $0.10 \times 0.03 \mu\text{m}$ ). The dark contrast of the inner material suggests that these inclusions are essentially fluid-free (that is, they are melt inclusions). The second kind is represented by ‘swarm-shaped’ trails, inclined by 30–40° with respect to the olivine [100] and consisting of inclusions with variable size and shape (Fig. 6b). Most of these inclusions are partially empty.

Negative crystals show perfectly formed crystal faces: for instance, Fig. 7 shows a detail of a prismatic negative crystal within olivine, with (010), (100) and (120) faces: the ordered structure of olivine

(the regular orthogonal array of spots) sharply interrupts at the negative crystal face boundary without any structural defect. This evidence indicates a mature state in the negative crystal evolution.

Common shapes and inner textures are sketched in Fig. 8 (as observed along the olivine [001]). (010) and (100) are the most important faces: in particular, (010) is always more developed than (100), especially in prismatic inclusions. (120), (110) and (130) are also common: the occurrence of the above faces well agrees with previous works on olivine crystal morphology (Fleet 1975; T’Hart 1987a,b). As previously stated, slight differences in size and shape could be due to different sections of the negative crystal along its [001] axis: however, this feature could not explain the wide range of observed shapes in these trails. It is worth of mention that negative crystals are often asymmetrical with respect to both (100) and (010) equatorial planes.

The relative growth of each face varies from inclusion to inclusion, even within the same trail. A possible explanation is that different shapes arise from local chemical differences in the trapped material (for instance, slightly different proportions among fluid phase, silicate and sulphide melts). A local enrichment in the fluid phase (giving rise to a more

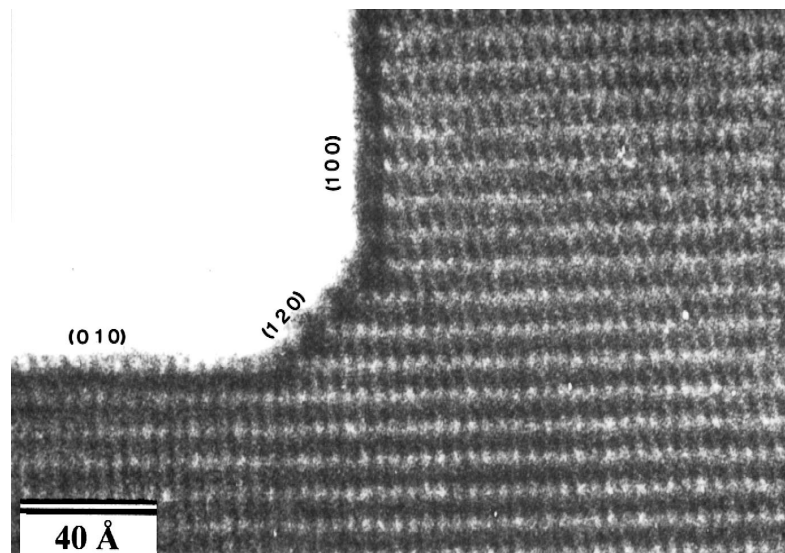


Fig. 7. Negative crystal in olivine: note that the structure of olivine is ordered even at the negative crystal faces. Same sample of Fig. 5.

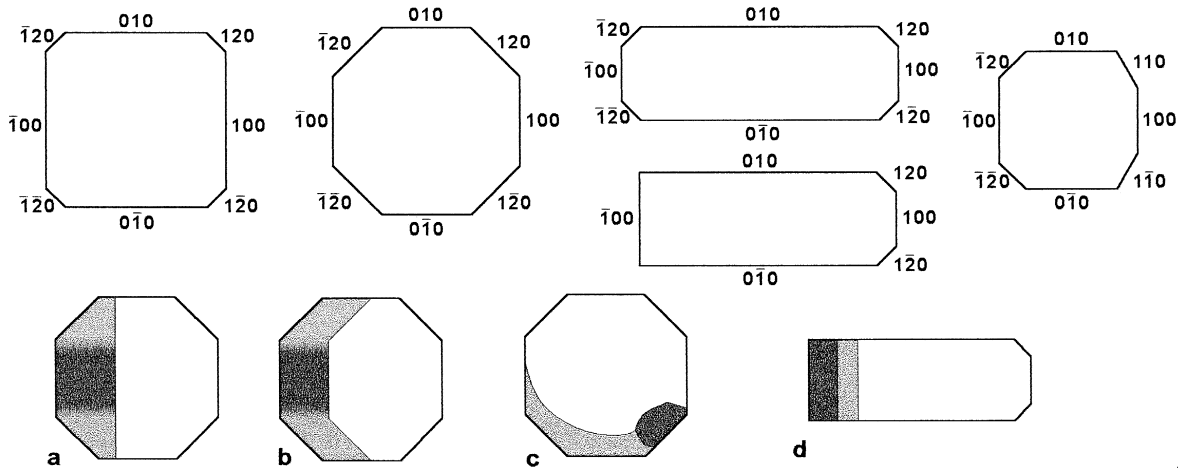


Fig. 8. Sketch of common shapes (with the corresponding crystal faces) and inner textures of negative crystals in olivine. Same sample of Fig. 5.

or less isotropic large bubble) could promote an equant growth of (010) and (100) faces, as commonly observed in swarm-shaped trails; by contrary, the trapping of essentially fluid-free viscous silicate–sulphide melts could give rise to prismatic negative crystals.

Inclusions may be empty, partially empty or full, with an inner textural arrangement variable from inclusion to inclusion. The study of the inner texture

is obviously complicated by sample preparation: in most of the fluid inclusions, the fluid phase is lost during thinning, whereas collapse may have affected the inner solid phases. Consequently, it is quite difficult to know the original composition of empty and partially empty inclusions.

In partially empty inclusions, the inner material can be indifferently concentrated at the (100) or at the (100) faces. It shows a strong contrast, often with

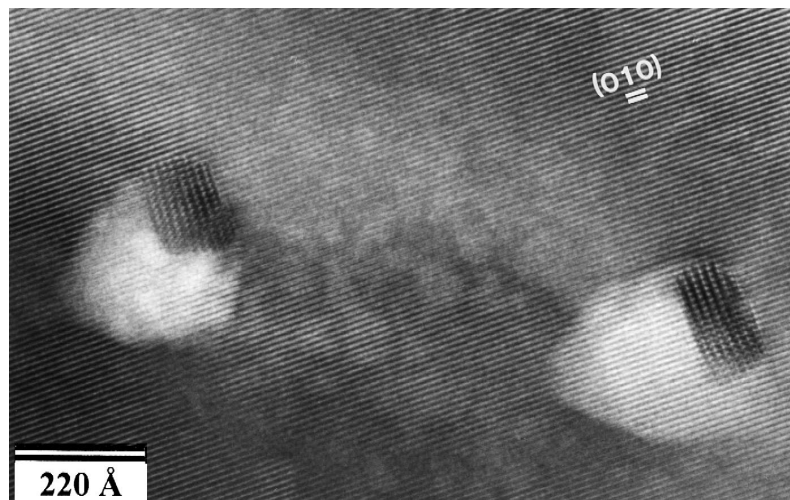


Fig. 9. Daughter minerals in inclusions. The interference between the (010) lattice fringes of olivine and the lattice fringes of the inner minerals gives rise to a 'Moiré pattern'. Same sample of Fig. 5.

a sort of internal zoning parallel to (100). The boundary between the inner material and the empty space can be parallel to (100), independently from the shape of the negative crystal (see Fig. 8, crystal a), or it can be exactly coherent with respect to the shape of the negative crystal (see Fig. 8, crystal b). The boundary can also appear as a regular meniscus

(see Fig. 8, crystal c), which suggests that this inclusion was originally filled by a fluid phase. The inner material often shows internal contrast heterogeneities, namely, dark faceted grains within a lighter, featureless material. Electron diffraction and high-resolution images may provide information on the structural state of these inner materials (in particular,

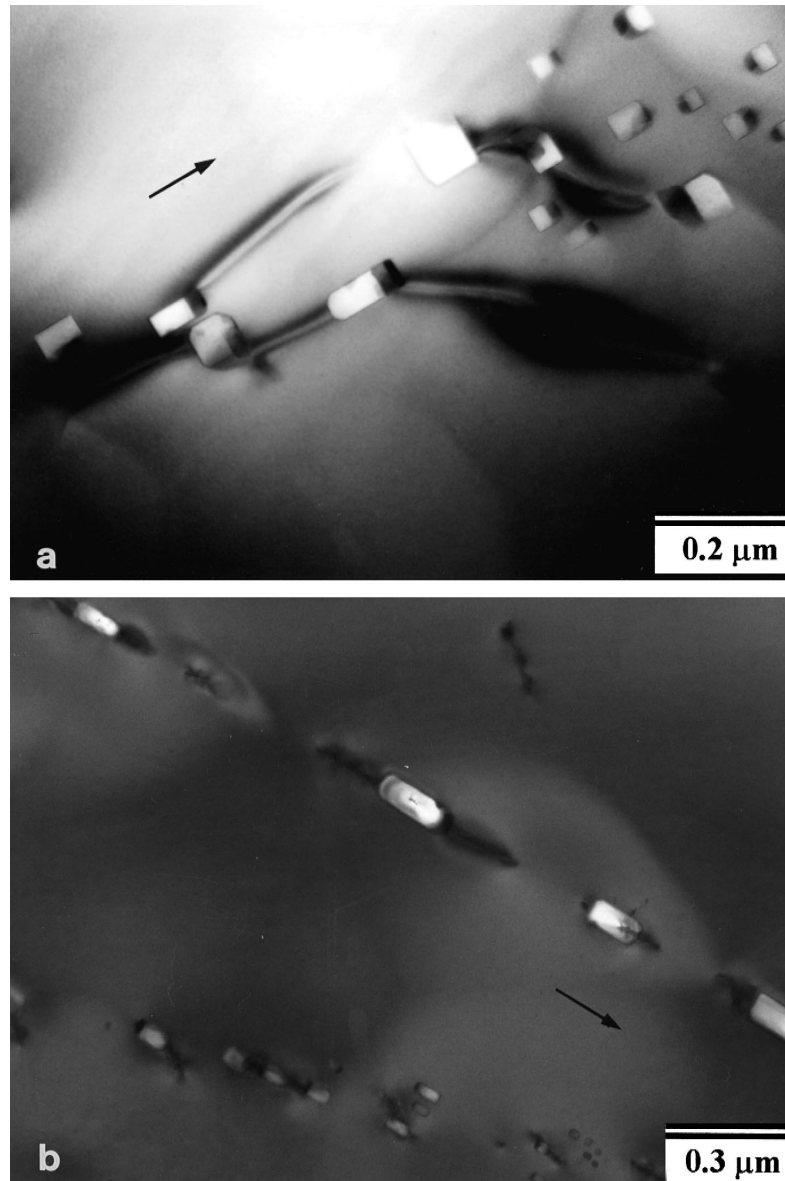


Fig. 10. (a) Sigmoidal tails connected to inclusions in swarm shaped trails. (b) Tails connected to prismatic inclusions in regular [100] trails. Arrows indicate olivine [100]. Same sample of Fig. 5.

glassy or crystalline). For example, the inner dark grains in Fig. 9 exhibit lattice fringes, interfering with the (010) lattice fringes of the host olivine: the occurrence of lattice fringes reveals the crystalline state of the inner daughter minerals (an iron–nickel sulphide from EDS analysis).

### 3.3. Re-equilibration features of fluid inclusions

TEM also provide information on the inclusion–host mineral relationships, revealing features as dislocations, fractures or other structural perturbations, connected to the inclusion. In many examples (both in olivine and in quartz), inclusions are connected to irregularly curved tails, often showing a sigmoidal pattern (Fig. 10a and b) and interpreted as dislocation arrays. A wide strain contrast field is typically associated to the tails, indicating that the host mineral structure is here widely disturbed. Each tail may be shared by two to three different inclusions. Fig. 11 shows a dislocation in olivine connected to a fluid inclusion. Similar features have been observed also in quartz: Fig. 12 shows negative crystal-like inclusions, occurring in a quartz grain approximately along [001] and connected to dislocations.

Most of these features (reactions, deformation and leakage of fluid inclusions) may often remain undetected at the OM scale (Andersen and Neumann,

2001). Consequently, possible misinterpretations can derive from measuring inclusions, which do not fit the definition of ‘closed isochoric system’. TEM investigation may help in identifying hidden re-equilibration features. Bakker and Jansen (1994) reported the occurrence of dislocations connected to mixed H<sub>2</sub>O–CO<sub>2</sub> fluid inclusions in synthetic quartz. The authors propose that over- and under-pressure of the fluid inclusions constitute a driving force for the development of dislocations and that preferential water leakage there occur. The preferential leakage of water is explained as due to the lower size of the H<sub>2</sub>O with respect to CO<sub>2</sub> (which can further react with water to form larger H<sub>2</sub>CO<sub>3</sub> molecules) and to the chemical affinity between the hydrophyle quartz and water.

Similar features (high dislocation density around fluid inclusions) have been also observed in natural quartz samples. For instance, deformed quartz (in veins from the blueschist of the Verrucano Formation, Southern Tuscany) contain abundant pure H<sub>2</sub>O inclusions (typically negative crystal-shaped) with no evidence, at the optical scale, for re-equilibration. During homogenization of these inclusions, spontaneous leakage often occurs before Th was reached. TEM observations revealed that dislocations are associated to these inclusions and that dislocations are mutually connected forming a network distribution of ‘open’ fluid inclusions (Fig. 12).

Dislocations may be also associated to inclusions in natural olivines. Fluid inclusions in xenolith olivines, carried rapidly by basaltic melts during volcanic eruption, provide the basis of our knowledge on the composition and density of fluids present at mantle depth. However, only very few fluid inclusions are representative of original trapping conditions in the upper mantle (e.g. Frezzotti et al., 1992; Neumann, 1991; Szabo and Bodnar, 1996), while the wide majority of inclusions commonly show re-equilibration of densities to lower values. We do not know if this spread of values has a petrogenetic significance (e.g. residence in magma chamber) or it indicates an open-system behavior for fluid inclusions (e.g. partial loss of fluid).

Early TEM studies (Green and Radcliffe, 1975) have shown that nanostructures and dislocations could have influenced the fluid inclusion ‘closed system’ by a leakage of CO<sub>2</sub>. Similar features have been

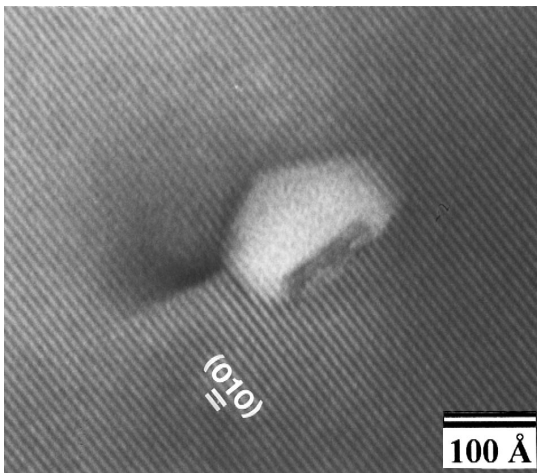


Fig. 11. Dislocation connected to an inclusion in olivine. Note also the inner dark faceted grain, possibly corresponding to a crystalline phase. Same sample of Fig. 5.

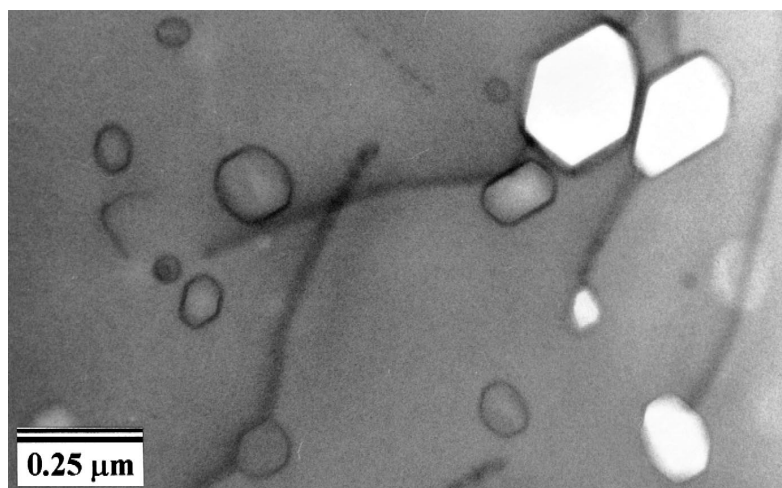


Fig. 12. Dislocations connected to negative crystals in quartz. Sample from a quartz vein in the Verrucano Formation (Southern Tuscany).

recently observed in xenolith olivines from Tenerife (Viti and Frezzotti, 2000). Previous fluid inclusion investigations showed that xenoliths were originated at great depth (corresponding to 6–10 kbar), even though most of fluid inclusions were re-equilibrated at lower densities (corresponding to 2–4 kbar). At the TEM scale, these fluid inclusions are connected to healed nanostructures and dislocation arrays (see, for instance, Figs. 10 and 11), which could have determined a fluid phase leakage. The CO<sub>2</sub> leakage could contribute to the variability on measured densities, as well as to the occurrence of very low-density values. Dislocations possibly occurred in mantle conditions: during the rapid ascent to the surface, fluid inclusions underwent internal overpressure, thus promoting the CO<sub>2</sub> leakage from these open systems.

#### 4. Summary and conclusions

Why do we use TEM in fluid inclusion investigation? In our opinion, there are at least three specific reasons: (1) imaging of defects, dislocations, strain fields, healed nanostructures connected to inclusions; study of the relations and boundaries between inclusions and host minerals; identification of possible opening processes, which are often undetected at the OM; (2) diffraction from very small volumes and high-resolution images, providing information on the structural state of the inner material (distinction be-

tween amorphous glass and crystalline daughter minerals); (3) analytical resolution which allows the obtaining of uncontaminated chemical data from a single inclusion (for instance, chemistry of melt inclusions, chemistry of daughter minerals, without contamination by the host mineral).

In particular, the knowledge of the host mineral–inclusion relation represents a fundamental point for the correct interpretation of fluid inclusions data (does the inclusion actually behave as a closed system?): TEM cannot be considered as a routine technique in fluid inclusion study, but it should be recommended in all cases where the textural characters and the density data from fluid inclusions are controversial.

#### References

- Akai, J., 1994. Void structures in olivine grains in thermally metamorphosed antarctic carbonaceous chondrite B-7904. *Proc. NIPR Symp. Antarct. Meteorites* 7, 94–100.
- Andersen, T., Neumann, E.-R., 2001. Fluid inclusions in mantle xenoliths. *Lithos* 55, 299–318 (this volume).
- Bakker, R.J., Jansen, J.B.H., 1994. A mechanism for preferential H<sub>2</sub>O leakage from fluid inclusions in quartz, based on TEM observations. *Contrib. Mineral. Petrol.* 116, 7–20.
- Buseck, P.R., Cowley, J., Eyring, L., 1988. *High Resolution Transmission Electron Microscopy and Associated Techniques*. Oxford Univ. Press.
- Buseck, P.R., 1992. Minerals and reactions at the atomic scale. *Mineral. Soc. Am. -Rev. Mineral.* 27, 508.

- Cliff, G., Lorimer, G.W., 1975. The quantitative analysis of thin specimens. *J. Microsc.* 103, 203–207.
- Cowley, J., 1981. *Diffraction Physics*. 2nd edn. North Holland, New York.
- Dorset, D., Hovmoller, S., Zou, X., 1997. Electron crystallography. *NATO ASI Ser.* 347, 439.
- FitzGerald, J.D., Boland, J.N., McLaren, A.C., 1991. Microstructures in water-weakened single crystals of quartz. *J. Geophys. Res.* 96, 2139–2155.
- Fleet, M., 1975. The growth habits of olivine — a structural interpretation. *Can. Mineral.* 13, 293–297.
- Frezzotti, M.-L., Burke, E.A.J., De Vivo, B., Stefanini, B., Villa, I.M., 1992. Mantle fluids in pyroxenite nodules from Salt Lake Crater (Oahu, Hawaii). *Eur. J. Mineral.* 4, 1137–1153.
- Gjønnes, J., 1997. Convergent beam electron diffraction: basic principles. *Electron Crystallography*. In: Dorset, D.L., Hovmoller, S., Zou, X. (Eds.), *NATO ASI Series* 347, 439 pp.
- Green, H.W., Radcliffe, S.V., 1975. Fluid precipitates in rocks from the Earth's mantle. *Geol. Soc. Am.* 86, 846–852.
- T'Hart, J.T., 1987a. The structural morphology of olivine: I. A qualitative derivation. *Can. Mineral.* 16, 175–186.
- T'Hart, J.T., 1987b. The structural morphology of olivine: II. A quantitative derivation. *Can. Mineral.* 16, 547–560.
- McLaren, A.C., Cook, R.F., Hyde, S.T., Tobin, R.C., 1983. The mechanism of the formation and growth of water bubbles and associated dislocation loops in synthetic quartz. *Phys. Chem. Miner.* 9, 79–94.
- Mellini, M., 1989. High resolution transmission electron microscopy and geology. *Advances in Electronics and Electron Physics*, vol. 76, pp. 281–326.
- Mellini, M., Menichini, R., 1985. Proportionality factors for thin film TEM/EDS microanalysis of silicate minerals. *Rend. Soc. Ital. Mineral. Petrol.* 40, 261–266.
- Neumann, E.R., 1991. Ultramafic and mafic xenoliths from Hierro Canary Islands: evidences for melt infiltration in the upper mantle. *Contrib. Mineral. Petrol.* 106, 236–252.
- O'Keefe, M.A., Buseck, P.R., Iijima, S., 1978. Computed crystal structure images for high resolution electron microscopy. *Nature*, 322–324.
- Peacor, D., 1992. Analytical electron microscopy: X-ray analysis. *Minerals and Reactions at the Atomic Scale*. In: Buseck, P.R. (Ed.), *Mineral. Soc. Am. -Rev. Mineral.*, p. 27.
- Self, P., 1992. High resolution image simulation and analysis. *Minerals and Reactions at the Atomic Scale*. In: Buseck, P.R. (Ed.), *Mineral. Soc. Am. -Rev. Mineral.* 27.
- Spence, J.C., 1981. *Experimental High Resolution Electron Microscopy*. Clarendon Press, Oxford.
- Steeds, J.W., Morniroli, J.P., 1992. Electron diffraction — SAED and CBED. *Minerals and Reactions at the Atomic Scale*. In: Buseck, P.R. (Ed.), *Mineral. Soc. Am. -Rev. Mineral.* 27.
- Szabo, C.S., Bodnar, R.J., 1996. Changing magma ascent rates in the Nograd–Gomor volcanic field Northern Hungary/Southern Slovakia: evidence from CO<sub>2</sub>-rich inclusions in metasomatised upper mantle xenoliths. *Petrol* 4, 240–249.
- Tanaka, M., 1997. Convergent beam electron diffraction. *Electron Crystallography*. In: Dorset, D.L., Hovmoller, S., Zou, X. (Eds.), *NATO ASI Series* 347, 439 pp.
- Veblen, D.R., 1985. Direct TEM imaging of complex structures and defects in silicates. *Annu. Rev. Earth Planet. Sci.* 13, 119–146.
- Viti, C., Frezzotti, M.L., 2000. Re-equilibration of glass and CO<sub>2</sub> inclusions in xenolith olivine: a TEM study. *Am. Mineral.* 85, in press.
- Williams, D.B., Carter, C.B., 1996. *Transmission Electron Microscopy — A Textbook for Material Science*. Plenum, New York.